

**Phase retrieval via SLM phase modulation in 4f optical
setup: numerical inverse imaging with sparse
regularization for phase and amplitude**

Vladimir Katkovnik and Jaakko Astola

Department of Signal Processing, Tampere University of Technology,

P. O. Box 553, Tampere, Finland, vladimir.katkovnik@tut.fi.

The 4f optical setup is considered with a wave field modulation by SLM (spatial light modulator) located in the focal plane of the first lens. Phase as well as amplitude of the wave field are reconstructed from noisy multiple intensity observations. The reconstruction is optimal due to a constrained maximum likelihood formulation of the problem. The proposed algorithm is iterative with decoupling of the inverse of the forward propagation of the wave field and the filtering of phase and amplitude. The *sparse* modeling of phase and amplitude enables the advanced high accurate filtering and sharp imaging of the complex-valued wave field. Artefacts typical for the conventional algorithms (wiggles, ringing, waves, etc.) and attributed to optical diffraction can be suppressed by the proposed algorithm. © 2011 Optical Society of America

OCIS codes: 070.2025, 100.3010, 100.3190, 100.5070

1. Introduction

Reconstructing phase of a coherent wave field from intensity measurements constitutes the *phase retrieval* problem. Multiple measurements gain an ob-

servation redundancy which can be exploited in order to reconstruct both amplitude and phase and to improve the accuracy. Various problems of wave field reconstruction from intensity measurements arise in optics, interferometry, phase microscopy, astronomy, crystallography, and other areas of physics and engineering.

In general, *phase diversity* assumes that registered multiple wave fields are specially modulated. If those modulations are known the corresponding wave field disturbances can be inverted and compensated in order to reconstruct the wave field of interest.

Defocusing is one of the popular ideas enabling the phase diversity. Recorded defocused images are then numerically processed to retrieve phase and amplitude information. First results based on this approach are demonstrated in 1973 by Misell [1] and in 1980 by Saxton [2] for two defocused images obtain using optical lens.

The defocusing can be achieved using displaced sensor planes. Then multiple intensity measurements constitute data for phase and wave field reconstruction. This approach is developed and studied by Pedrini, et al. [3], Almoró, et al. [4] and [5]. In the recent development, in particular we refer

to Kohler, et al. [6] and Camacho, et al. [7], a spatial light modulator (SLM) is exploited in order to get a set of differently defocused images.

The phase diversity can be achieved also by methods which are different from the straightforward defocusing (e.g. [8,9]). The phase modulation in the Fourier plane of $4f$ optical system is used in the phase contrast microscopy in order to transform the invisible phase object distribution in the visible image magnitude. This revolutionary technique invented by Zernike in the 1930s (Nobel prize 1953) is widely exploited to provide contrast to transparent specimens such as living cells or small organisms. Modern developments of this technique with various applications are presented in the book by Glückstad and Palima [10].

Recently, a phase retrieval technique, based on SLM in the Fourier domain of $4f$ imaging system, has been proposed by Falldorf, et al. [11]. The SLM phase modulation imitates parallel displacements of the sensor plane. This development aggregates the phase contrast imaging and defocusing by varying distances between the object and sensor planes.

Concerning numerical algorithms for the phase retrieval first of all we wish to mention the Gerchberg-Saxton-Fienup (GSF) techniques (e.g. [12–14]). For

the multiple plane intensity measurements this type of the algorithms has been developed by Ivanov, et al. [15] and Pedrini, et al. [16]. An enhanced version of the latter technique is produced by Almoró, et al. [4,5]. These algorithms, known as single-beam multiple-intensity reconstruction (SBMIR), start from an initial guess of the complex amplitude at the first measurement plane. Then, this initial guess propagates numerically forward from the one measurement plane to the next following one successively through the all sequence of the recordings. At each plane the calculated modulus of the wave field is replaced by the square root of the intensity measured for this plane. When the last measurement plane is reached the wave field estimate at this plane is propagated back to the first plane. This iterative process is repeated until convergence.

Contrary to these intuitively clear heuristic algorithms the variational approaches as a rule have a strong mathematical background and start from formulation of the objective function (criterion), usually probabilistic, and restrictions incorporating a prior information on the wave field of interest. The algorithm design is produced by solving an optimization problem.

There are many publications concerning variational techniques as well as

revisions of the intuitive algorithms by using optimizational formulations. In particular, the links between the conventional GSF and variational techniques are studied in [17]. A sophisticated variational formulation for the phase retrieval is demonstrated by Irwan and Lane [18], where the criterion corresponding to Poissonian observations and the prior defining the smoothness of the phase are proposed. The problem is formalized as a penalized likelihood optimization. The conjugate gradient iterative algorithm for this setting is proposed by Lane [19].

Sparse approximations is a recent trend in image processing. It can be treated as a special regularization technique where regularization is introduced through a *sparse* image modeling. It is assumed in *sparse imaging* that there exists a basis consisting of a small number of items where the image can be represented exactly or approximately with high accuracy. This *ideal* basis is a priori unknown and selected from a given set of potential bases (dictionary or dictionaries). The great popularity and success of *sparse imaging* are due to the attractive theory, the efficient algorithms and the evidence that the developed formalism fits perfectly to many important applications.

The *compressive* (or *compressed*) sensing (*CS*) is one of the fields where

the *sparse imaging* techniques are efficient. In CS the image is reconstructed from subsampled data. A total number of available observations can be smaller (much smaller) than size of the image. It is proved in CS that the perfect reconstruction from the subsampled data can be achieved for *sparse object distributions* [20–22].

Recently in optics, *sparse imaging* has become a subject of multiple applications in the context of CS. Complex-valued signals and operators are distinctive features of this development of CS. Basic facts of the corresponding theory, algorithms, simulations as well as experimental demonstrations are presented by Gazit et. al [23], where CS is used for sub-wavelength imaging overcoming the diffraction limitations. The penalization (regularization) for variational image reconstructions in [23] are formulated using the l_0 - and l_1 -norms for spectra of object representations.

We wish to mention also few works on CS which are relevant to our paper. A slice-by-slice reconstruction of a 3D object from the holographic data is considered by Brady et. al [24] and by Cull et. al [25]. In the work by Choi et. al [26] a maximum likelihood approach is developed for estimation of the object density from 2D scattered fully developed speckle field measurements.

The total variation (TV) penalization is exploited as a regularization tool in this inverse imaging. A compressive Fresnel holography in the paper by Rivenson et. al [27] is considered using a combination of two types of the penalties l_1 -norm and TV.

It is assumed in the cited papers that the wave field is modeled as a linear combination of basis functions. Phase and amplitude signals are mixed together in these approximations. In particular, in [23] the phase issue appears only as a sign of the real-valued wave field distribution. The reconstruction of a full range of phase values is not considered.

In our opinion, the only way to the high-accuracy reconstruction is a non-linear modeling of the wave field with a separate approximation (modeling) for phase and amplitude.

At this point we refer to the work by Xu and Lam [28], where a strong improvement in CS hyperspectral imaging is demonstrated due to the quadratic penalization for phase used jointly with the total variation penalty for the complex-valued wave field. This is a good example of an efficient penalization separate for phase and amplitude.

In this paper we develop a general approach to wave field reconstruction

using a high-order adaptive approximation for phase and amplitude. The rest of the paper is organized as follows. In Section 2 the image formation in $4f$ optical system and the observation model are presented. The sparse modeling for phase and amplitude are introduced in Section 3. The constrained variational approach for the phase retrieval is presented in Section 4. The proposed algorithm is presented in Section 5. Simulation experiments are shown and discussed in Section 7. The mathematical proofs are presented in Appendices I and II.

2. Observation model

In this section we derive the image formation model linking complex amplitudes at the object and image planes. It is assumed that the wave field is coherent and the Fresnel approximation is used for its modeling. The considered $4f$ configuration of the optical system is shown in Fig. 1.

2.A. Continuous modeling

Let $u_0(x)$ and $u_r(x)$, $x = (x_1, x_2)$, denote, respectively, complex wave field distributions at the object and parallel image planes with distance $4f$ between the planes (Fig. 1).

The Fourier transforms of $u_0(x)$ and $u_r(x)$ are denoted by the corresponding capital letters with the argument v for frequency. For instance, $U_0(v) = \mathcal{F}_x\{u_0(x)\}(v) = \int_{\mathbb{R}^2} u_0(x) \exp(-2\pi j(v, x)) d^2x$, where $d^2x = dx_1 dx_2$ and (v, x) stands for the inner product of the vectors $v, x \in \mathbb{R}^2$, and \mathcal{F}_x means that the Fourier transform is calculated with respect to the variable x . The similar notation is used for the Fourier transform of all variables. For signals in the object and image planes we use as arguments the variable $x = (x_1, x_2)$ and for the Fourier plane the variable $v = (v_1, v_2)$.

Assume that the optical mask inserted at the Fourier plane has a complex-valued transmittance $M_r(v)$, where $v \in \mathbb{R}^2$ is the frequency variable.

For the paraxial approximation the wave field in the Fourier plane of the first lens is calculated as ([29], page 106):

$$c(\nu) = \frac{1}{j\lambda f} \mathcal{F}_x\{u_0(x)\}\left(\frac{\nu}{\lambda f}\right) = \frac{1}{j\lambda f} U_0\left(\frac{\nu}{\lambda f}\right). \quad (1)$$

In what follows the index in \mathcal{F}_x and the argument of the Fourier transform can be omitted when they are obvious. Note that the constant phase factor is neglected in Eq. (1).

Then, the wave field distribution immediately after the mask is equal to the product $a(\nu) \cdot M_r(v)$, and once more using Eq. (1) the wave field at the

image plane is calculated as

$$u_r(x) = \frac{1}{j\lambda f} \mathcal{F}_v \{c(\nu) \cdot M_r(\nu)\} \left(\frac{x}{\lambda f}\right). \quad (2)$$

Inserting Eq. (1) into Eq. (2) after some manipulations we obtain for the Fourier transform of $u_r(x)$:

$$U_r(\nu) = -U_0(-\nu)M_r(-\lambda f \cdot \nu). \quad (3)$$

Eq. (3) defines the continuous input-output model for the $4f$ optical system from the object to the image planes linking the corresponding input and output complex-valued distributions $u_0(x)$ and $u_r(x)$. The model (3) is valid for an arbitrary complex-valued transmittance M_r .

2.B. Discrete modeling

In discrete modeling the continuous argument x is replaced by the digital one with a corresponding replacement of all continuous functions by their discrete counterparts: $u_0(x_1, x_2) \rightarrow u_0(\Delta_{x_1}k_1, \Delta_{x_2}k_2) \triangleq u_0[k]$, $u_z(x_1, x_2) \rightarrow u_z(\Delta_{x_1}k_1, \Delta_{x_2}k_2) \triangleq u_z[k]$ with $2D$ integer argument $k = (k_1, k_2)$. This discretization assumes that wave field distributions are pixelated, i.e. pixel-wise invariant with pixels $\Delta_{x_1} \times \Delta_{x_2}$ for the object and image planes. Pixels of a different size $\Delta_{v_1} \times \Delta_{v_2}$ are assumed for the Fourier plane with the corre-

sponding pixelated variables $c(v_1, v_2) \rightarrow c(\Delta_{v_1} l_1, \Delta_{v_2} l_2) \triangleq c[l]$, $l = (l_1, l_2)$.

For discrete modeling we use 2D Fast Fourier Transform (FFT) conventionally defined as

$$U_0[l_1, l_2] = \mathcal{F}\mathcal{F}\mathcal{T}\{u_0[k_1, k_2]\} \triangleq \quad (4)$$

$$\sum_{k_1=0}^{N_1-1} \sum_{k_2=0}^{N_2-1} u_0[k_1, k_2] \exp(-j2\pi(k_1 l_1/N_1 + k_2 l_2/N_2)),$$

$$u_0[k_1, k_2] = \mathcal{F}\mathcal{F}\mathcal{T}^{-1}\{U_0[l_1, l_2]\} \triangleq \quad (5)$$

$$\frac{1}{N_1 N_2} \sum_{l_1=0}^{N_1-1} \sum_{l_2=0}^{N_2-1} U_0[l_1, l_2] \exp(j2\pi(k_1 l_1/N_1 + k_2 l_2/N_2)),$$

where N_1 and N_2 define the image size with respect to variables k_1, k_2 respectively, and l_1, l_2 are the integer FFT frequencies, $0 \leq l_i \leq N_i - 1$, $i = 1, 2$.

Similar notation is used for FFT of all variables, in particular, FFT for $c(\nu)$ is defined as $C[l_1, l_2] = \mathcal{F}\mathcal{F}\mathcal{T}\{c[k_1, k_2]\}$.

We assume that the images at the object, Fourier and image planes are of the same size in pixels, $N_1 \times N_2$.

Let us assume that the following conditions are fulfilled

$$\frac{\Delta_{x_1} \Delta_{v_1}}{\lambda f} = \frac{1}{N_1}, \quad \frac{\Delta_{x_2} \Delta_{v_2}}{\lambda f} = \frac{1}{N_2}. \quad (6)$$

Then,

$$U_r[l_1, l_2] = -U_0[-l_1 + N_1, -l_2 + N_2] \cdot M_r[-l_1 + N_1, -l_2 + N_2], \quad (7)$$

$$0 \leq l_i \leq N_i - 1, \quad i = 1, 2.$$

Eq. (7) is derived in Appendix 1. It defines the discrete input-output model for the considered $4f$ optical system. This model is different from the continuous model (3), where the argument of the mask M_r is scaled with the parameter λf . There is no this kind of scaling in Eq. (7) due to the assumption (6).

It is convenient to introduce the variables \tilde{U}_0, \tilde{M}_r , such that

$$\tilde{U}_0[l_1, l_2] = -U_0[-l_1 + N_1, -l_2 + N_2], \quad (8)$$

$$\tilde{M}_r[l_1, l_2] = M_r[-l_1 + N_1, -l_2 + N_2],$$

and rewrite the discrete observation model (7) in the form

$$U_r[l_1, l_2] = \tilde{U}_0[l_1, l_2] \cdot \tilde{M}_r[l_1, l_2], \quad (9)$$

$$0 \leq l_i \leq N_i - 1, \quad i = 1, 2.$$

2.C. Observation model

Assume that we have a set of K experiments produced with different masks $M_r, r = 1, \dots, K$. The problem is to reconstruct a complex-valued object wave

field $u_0[k_1, k_2]$ from multiple noisy intensity observations $o_r[k_1, k_2]$ recorded at the image plane:

$$o_r[k_1, k_2] = |u_r[k_1, k_2]|^2 + \sigma_r \varepsilon_r[k_1, k_2], \quad r = 1, \dots, K, \quad (10)$$

where $|u_r[k_1, k_2]|^2$ is the intensity corresponding to the signal generated from the object distribution, and the noise is zero-mean Gaussian with the variance σ_r^2 , $\varepsilon_r[k_1, k_2] \sim \mathcal{N}(0, 1)$, independent for different (k_1, k_2) and r .

Thus, the observations (10) are given on the regular discrete grid, $0 \leq k_i \leq N_i - 1$, $i = 1, 2$, corresponding to the digital sensor located at the image plane.

3. Sparse phase and amplitude modeling

In what follows we use a vector-matrix notation \mathbf{u}_0 for the object wave field, where $N_1 \times N_2$ image u_0 is given as a vector in \mathbb{C}^n , $n = N_1 N_2$. Here \mathbb{C}^n stands for the space of complex-valued vectors of the length n . This vector is obtained from the standard matrix representation for images by concatenating the columns of these matrices. We use bold lower case characters for this vector. The similar vector notation is used for phase and amplitude of u_0 . Thus, $\text{abs}(\mathbf{u}_0)$ and $\text{angle}(\mathbf{u}_0)$ are vectorial representations for phase and amplitude. Then, $\mathbf{u}_0 = \text{abs}(\mathbf{u}_0) \circ \exp(j2\pi \text{angle}(\mathbf{u}_0))$. In this formula (\circ) stands for the

Hadamard (elementwise) product of two vectors.

3.A. *Sparse approximations and frames*

Let \mathbf{Y} be a vector representation of phase or amplitude. *Sparse approximations* for \mathbf{Y} can be given in *synthesis* and *analysis* forms, respectively, as follows:

$$\mathbf{Y} = \mathbf{\Psi}\boldsymbol{\theta} \tag{11}$$

and

$$\boldsymbol{\theta} = \mathbf{\Phi}\mathbf{Y}. \tag{12}$$

Here, $\mathbf{Y} \in \mathbb{R}^n$, $\boldsymbol{\theta} \in \mathbb{R}^m$, and $\mathbf{\Psi}$ and $\mathbf{\Phi}$ are transform matrices of the corresponding sizes, $n \times m$ and $m \times n$, respectively. The vector $\boldsymbol{\theta}$, usually called *spectrum*, gives the parameters for the parametric approximation of the image \mathbf{Y} as $\mathbf{Y} = \mathbf{\Psi}\boldsymbol{\theta}$. Thus, $\mathbf{Y} = \sum_{j=1}^m \mathbf{\Psi}_j \cdot \theta_j$, where $\mathbf{\Psi}_j$ are the columns of the matrix $\mathbf{\Psi}$, and θ_j are the items of the vector $\boldsymbol{\theta}$.

If the synthesis defines the image provided that the spectrum is given, $\mathbf{Y} = \mathbf{\Psi}\boldsymbol{\theta}$, the analysis defines the spectrum corresponding to a given image as $\boldsymbol{\theta} = \mathbf{\Phi}\mathbf{Y}$.

It is recognized that overcomplete representations for \mathbf{Y} with $m \gg n$ and linearly dependent $\mathbf{\Psi}_j$ form a much more powerful tool for advanced imaging

than the classical orthonormal bases with $m = n$.

The concept of *frame* is a generalization of these classical bases developed for overcomplete (synthesis and analysis) representations with linearly dependent approximating functions (e.g. [30]).

There are special links between the analysis and synthesis frames. The requirement, $\Psi \cdot \Phi = \mathbf{I}_{n \times n}$, where $\mathbf{I}_{n \times n}$ is the $n \times n$ identity matrix, enables a perfect reconstruction of any \mathbf{Y} from the corresponding spectrum $\boldsymbol{\theta}$, indeed $\mathbf{Y} = \Psi \boldsymbol{\theta} = \Psi \cdot \Phi \mathbf{Y} = \mathbf{Y}$. For the so-called *tight* frames, $\Phi^T \cdot \Phi = \mathbf{I}_{n \times n}$ and $\Psi = \Phi^T$ [30].

For details and applications of overcomplete, in particular, frame based modeling for imaging we refer to the recent books [31, 32].

3.B. Sparse approximations for phase and amplitude

Modeling of the object wave field lies at the core of variational approaches to wave field imaging. A complex-valued wave field requires distinct modeling for amplitude and phase.

In this paper we apply frames for a sparse modeling of both phase (*angle*) and amplitude (*modulus*) of \mathbf{u}_0 . The following synthesis and analysis equations link amplitude and phase with the corresponding transform (spectrum)

representations:

$$\text{abs}(\mathbf{u}_0) = \mathbf{\Psi}_a \boldsymbol{\theta}_a, \text{ angle}(\mathbf{u}_0) = \mathbf{\Psi}_\varphi \boldsymbol{\theta}_\varphi, \quad (13)$$

$$\boldsymbol{\theta}_a = \mathbf{\Phi}_a \cdot \text{abs}(\mathbf{u}_0), \boldsymbol{\theta}_\varphi = \mathbf{\Phi}_\varphi \cdot \text{angle}(\mathbf{u}_0), \quad (14)$$

where $\boldsymbol{\theta}_a$ and $\boldsymbol{\theta}_\varphi$ are vectors of the amplitude and phase spectra. The modulus and angle operations applied to vectors in Eqs. (13)-(14) are elementwise. Thus, $\text{abs}(\mathbf{u}_0)$ and $\text{angle}(\mathbf{u}_0)$ are vectors of amplitude and phase values.

The *frame* synthesis and analysis matrices $\mathbf{\Psi}_a$, $\mathbf{\Phi}_a$, $\mathbf{\Psi}_\varphi$, $\mathbf{\Phi}_\varphi$ are shown with the indices a and φ for amplitude and phase, respectively.

Eqs. (13) define the synthesis giving amplitude ($\text{abs}(\mathbf{u}_0)$) and phase ($\text{angle}(\mathbf{u}_0)$) from the amplitude and phase spectra $\boldsymbol{\theta}_a$ and $\boldsymbol{\theta}_\varphi$. On the other hand, the analysis Eqs. (14) give the spectra for amplitude and phase of \mathbf{u}_0 .

Using the synthesis formulas we have

$$\mathbf{u}_0 = \mathbf{\Psi}_a \boldsymbol{\theta}_a \circ \exp(j \mathbf{\Psi}_\varphi \boldsymbol{\theta}_\varphi). \quad (15)$$

Eq. (15) is the synthesis equations (13) given in the complex-valued form.

The l_0 -norm of the vector $\boldsymbol{\theta}$, denoted by $\|\boldsymbol{\theta}\|_0$, is defined as a number of nonzero elements of the vector. The l_1 -norm of $\boldsymbol{\theta}$ is defined as the sum of absolute values of items of this vector, $\|\boldsymbol{\theta}\|_1 = \sum_s |\boldsymbol{\theta}_s|$. Both these norms are

used in order to characterize *sparsity* of approximation. A smaller value of the norm means a higher sparsity of approximation.

It is known, that the variational image reconstructions using l_0 and l_1 -norms as penalties, provided some assumptions, give results that are close to each other. This is an important fact, because it allows to replace the non-convex l_0 -norm by the convex l_1 -norm in many variational settings [31] and [32].

In our approach the sparsity is evaluated separately for phase and amplitude by the l_p -norms, $\|\boldsymbol{\theta}_\varphi\|_p$ and $\|\boldsymbol{\theta}_a\|_p$, where $p = 0, 1$ for the l_0 - and l_1 -norms, respectively. Overall, the main intention is to find sparsest (shortest) models for phase and amplitude with smallest values of the l_p -norms.

Recently a family of the Block Matching 3-D (BM3D) algorithms for various imaging problems has been developed within the framework of nonlocal patch-wise image modeling (e.g. Dabov et. al [33], Katkovnik et. al [34]). It is demonstrated by Danielyan et. al [35] and by Katkovnik et. al [36] that the BM3D filtering allows a frame interpretation and the analysis and synthesis frames are constructed, which are called BM3D-frames. These BM3D-frames are used to construct $\boldsymbol{\Psi}_a, \boldsymbol{\Phi}_a, \boldsymbol{\Psi}_\varphi, \boldsymbol{\Phi}_\varphi$ and to obtain the corresponding spec-

tra for phase and amplitude. We do not discuss details of the BM3D imaging in this paper and wish to mention only that BM3D frames are data adaptive and provide rich classes of atomic functions enabling good approximations for any complex images.

The sparse modeling for phase and amplitude using frames, in particular BM3D-frames, is developed in [37] for wave field reconstruction from complex-valued observations for the lensless scenario. In the current paper we generalize this technique for wave field reconstruction from multiple intensity observations in the 4f optical setup.

4. Variational formulation

4.A. Objective function and constraints

For the Gaussian noise distribution in Eq. (10) and sparse modeling for phase and amplitude the maximum likelihood approach leads to the following basic objective function

$$J = \sum_{r=1}^K \frac{1}{2\sigma_r^2} \sum_k (o_r[k] - |u_r[k]|^2)^2 + \tau_\varphi \cdot \|\boldsymbol{\theta}_\varphi\|_{l_p} + \tau_a \cdot \|\boldsymbol{\theta}_a\|_{l_p}, \quad (16)$$

where \sum_k stands for $\sum_{k_1=0}^{N_1-1} \sum_{k_2=0}^{N_2-1}$, and $\tau_a, \tau_\varphi > 0$ are regularization parameters.

The first summand in Eq. (16) is the quadratic fidelity term obtained

from the Gaussian likelihood function. The joint probability density of the independent observations (10) within a constant factor is equal to $\Pi_r \Pi_k \exp(\frac{-1}{2\sigma_r^2}(o_r[k] - |u_r[k]|)^2)$. The minus logarithm of this function gives the fidelity term in Eq. (16). The second and third terms in Eq. (16) are the penalty (regularization) terms defining the complexity (sparsity) of the models for phase and amplitude.

Due to (9), the link between u_r and u_0 is given by the equation

$$u_r[k] = \mathcal{F}\mathcal{F}\mathcal{T}^{-1}\{U_r[l]\} = \mathcal{F}\mathcal{F}\mathcal{T}^{-1}\{\tilde{U}_0[l] \cdot \tilde{M}_r[l]\}. \quad (17)$$

The links between the spectra θ_φ , θ_a and \tilde{u}_0 are given by the equations (13), (14), where \mathbf{u}_0 is replaced by $\tilde{\mathbf{u}}_0$.

These equations (13), (14) and (17) define the joint constraints of the wave field reconstruction problem.

In this paper following to [37], we propose an algorithm based on the multi-objective optimization. This technique is very different from the conventional single-objective optimization. The motivations of this approach are as follows:

(A) The algorithm produces a better imaging and better accuracy than algorithms based on the single-objective optimization.

(B) The algorithm is simple in implementation because the inversion and

the filtering operations are decoupled. An efficient procedure based on FFT is developed for the inversion, and an efficient algorithm based of hard- and soft- thresholding is developed for the phase and amplitude filtering.

4.B. Multi-objective optimization

Let us introduce the following two objective function:

$$\mathcal{L}_1(\tilde{u}_0, \{u_r\}, \boldsymbol{\theta}_a, \boldsymbol{\theta}_\varphi) = \quad (18)$$

$$\sum_{r=1}^K \frac{1}{2\sigma_r^2} \sum_k (o_r[k] - |u_r[k]|^2)^2 + \quad (19)$$

$$\sum_{r=1}^K \frac{1}{\gamma_r} \sum_k |u_r[k] - \mathcal{F}\mathcal{F}\mathcal{T}^{-1}\{\tilde{U}_0[l] \cdot \tilde{M}_r[l]\}|^2 +$$

$$\frac{1}{\gamma_0} \|\tilde{\mathbf{u}}_0 - \Psi_a \boldsymbol{\theta}_a \circ \exp(j\Psi_\varphi \boldsymbol{\theta}_\varphi)\|_2^2, \quad (20)$$

and

$$\mathcal{L}_2(\tilde{\mathbf{u}}_0, \boldsymbol{\theta}_a, \boldsymbol{\theta}_\varphi) = \tau_a \cdot \|\boldsymbol{\theta}_a\|_0 + \tau_\varphi \cdot \|\boldsymbol{\theta}_\varphi\|_0 + \quad (21)$$

$$\frac{1}{2\gamma_a} \|\boldsymbol{\theta}_a - \Phi_a \text{mod}(\tilde{\mathbf{u}}_0)\|_2^2 + \frac{1}{2\gamma_\varphi} \|\boldsymbol{\theta}_\varphi - \Phi_\varphi \text{angle}(\tilde{\mathbf{u}}_0)\|_2^2, \quad (22)$$

where $\|\cdot\|_2^2$ stands for the Euclidean norm of the vector.

The first summand in Eq. (18) is the fidelity term from Eq. (16). The second summand (19) and third summands (20) are the constraints (17) and (13) given using the quadratic penalization functions. γ_r and γ_0 are parameters of

this penalization. Recall, that Eq. (13) gives the synthesis constraints. Here $\tilde{\mathbf{u}}_0$ is the vectorized representation for the image \tilde{u}_0 and $\boldsymbol{\theta}_a, \boldsymbol{\theta}_\varphi$ are the spectra obtained for \tilde{u}_0 .

Two summands (21) define the complexity (sparsity) of the models for phase and amplitude as it is Eq. (16). Two summands (22) are the analysis constraints (14) given using the quadratic penalization functions. The quadratic penalization of constraint-equations is the usual practice in order to reduce the constrained optimization to an unconstrained one. Smaller values of the corresponding penalization parameters $(\gamma_r, \gamma_0, \gamma_a, \gamma_\varphi)$ mean that in the solution the corresponding equations will be fulfilled more accurately [41].

The objective functions \mathcal{L}_1 and \mathcal{L}_2 include the items of the criterion (16) as well as the all constraints linking the variables of the problem. A single-objective minimization could be formulated as minimization of the sum $\mathcal{L}_1 + \mathcal{L}_2$.

Following to the approach developed in [36] and [37] instead of this single-objective minimization we use the alternating minimization of \mathcal{L}_1 and \mathcal{L}_2 , provided that \mathcal{L}_1 is minimized with respect to $\tilde{u}_0, \{u_r\}$ and \mathcal{L}_2 is minimized with respect to $\boldsymbol{\theta}_a, \boldsymbol{\theta}_\varphi$.

It results in the following iterative algorithm:

$$\tilde{u}_0^{t+1} = \arg \min_{\tilde{u}_0, \{u_r\}} \mathcal{L}_1(\tilde{u}_0, \{u_r\}, \boldsymbol{\theta}_a^t, \boldsymbol{\theta}_\varphi^t), \quad (23)$$

$$(\boldsymbol{\theta}_a^{t+1}, \boldsymbol{\theta}_\varphi^{t+1}) = \arg \min_{\boldsymbol{\theta}_a, \boldsymbol{\theta}_\varphi} \mathcal{L}_2(\tilde{\mathbf{u}}_0^{t+1}, \boldsymbol{\theta}_a, \boldsymbol{\theta}_\varphi). \quad (24)$$

In Eq. (23) minimization of \mathcal{L}_1 on \tilde{u}_0 inverts the forward propagation operators from \tilde{u}_0 to u_r ; minimization of \mathcal{L}_1 with respect to the intermediate variables u_r agrees the observations $o_r[k]$ with the prediction of u_r obtained from \tilde{u}_0 due to Eq. (17). It filters noise in the observations $o_r[k]$. Minimization of \mathcal{L}_2 on $\boldsymbol{\theta}_a$ and $\boldsymbol{\theta}_\varphi$ filters phase and amplitude in the object wave field.

Thus, in the proposed algorithm inverse and filtering operations are decoupled. Instead of minimization of a single objective function the algorithm (23)-(24) is looking for a quite different solution which is a *fixed-point* $(\boldsymbol{\theta}_a^*, \boldsymbol{\theta}_\varphi^*, \tilde{\mathbf{u}}_0^*)$ defined by the equations:

$$\tilde{u}_0^* = \arg \min_{\tilde{u}_0, \{u_r\}} \mathcal{L}_1(\tilde{u}_0, \{u_r\}, \boldsymbol{\theta}_a^*, \boldsymbol{\theta}_\varphi^*), \quad (25)$$

$$(\boldsymbol{\theta}_a^*, \boldsymbol{\theta}_\varphi^*) = \arg \min_{\boldsymbol{\theta}_a, \boldsymbol{\theta}_\varphi} \mathcal{L}_2(\tilde{\mathbf{u}}_0^*, \boldsymbol{\theta}_a, \boldsymbol{\theta}_\varphi).$$

This fixed-point balances two different intentions: minimization of the fidelity term (accuracy of observation fitting) and the complexity of the used model (defined as $\tau_\varphi \cdot \|\boldsymbol{\theta}_\varphi\|_{l_p} + \tau_a \cdot \|\boldsymbol{\theta}_a\|_{l_p}$), provided the given restrictions.

5. Proposed algorithm

In presentation of the algorithm we exploit wave fields given in three different forms: in image domain ($u_r[k]$ and $\tilde{u}_0[k]$), in the 2D FFT domain ($U_r[l]$ and $\tilde{U}_0[l]$) and as the vectorized object image variable $\tilde{\mathbf{u}}_0$.

Using the solutions for the optimization problems (23)-(24) derived in Appendix II the successive steps of the proposed iterative algorithm are as fol-

lows:

4f-SPAR algorithm

$$\text{Input : } o_r[k], \tilde{M}_r[l], \tilde{u}_0^{init}[k] \quad (26)$$

$$\text{Using } \tilde{u}_0^{init} \text{ construct } \Phi_\varphi, \Phi_a \text{ and } \Psi_\varphi, \Psi_a \quad (27)$$

$$\text{Set } t = 0, \tilde{u}_0^0 = \tilde{u}_0^{init}, \tilde{v}_0^0 = \tilde{u}_0^{init} \quad (28)$$

Repeat until convergence:

$$1. U_r^{t+1/2}[l] = \tilde{M}_r^*[l] \tilde{U}_0^t[l], \quad (29)$$

$$2. u_r^{t+1}[k] = \mathcal{G}(o_r[k], u_r^{t+1/2}[k]), \quad (30)$$

$$3. \tilde{U}_0^{t+1}[l] = \frac{1}{\sum_{r=1}^K \frac{1}{\gamma_r} + \frac{1}{\gamma_0}} \times \quad (31)$$

$$\left(\sum_{r=1}^K \frac{1}{\gamma_r} \tilde{M}_r^*[l] U_r^{t+1}[l] + \frac{1}{\gamma_0} \tilde{V}_0^t[l] \right),$$

$$4. \theta_a^{t+1} = \mathfrak{Ih}_{\tau_a \gamma_a} (\Phi_a \cdot \text{mod}(\tilde{\mathbf{u}}_0^{t+1})), \quad (32)$$

$$5. \theta_\varphi^{t+1} = \mathfrak{Ih}_{\tau_\varphi \gamma_\varphi} (\Phi_\varphi \cdot \text{angle}(\tilde{\mathbf{u}}_0^{t+1})), \quad (33)$$

$$6. \tilde{\mathbf{v}}_0^{t+1} = \Psi_a \theta_a^{t+1} \circ \exp(j \Psi_\varphi \theta_\varphi^{t+1}), \quad (34)$$

$$t = t + 1.$$

The input variables of the algorithm are the intensity observations $o_r[k]$, the phase masks $\tilde{M}_r(l)$ and the initial guess \tilde{u}_0^{init} for the complex-valued object

distribution \tilde{u}_0 .

At the initialization stage (27) the amplitude and phase frames (transforms) Φ_φ , Φ_a and Ψ_φ , Ψ_a are constructed for phase and amplitude of \tilde{u}_0^{init} .

In the algorithm the upper index ' t ' stands for the iteration number. The iterations are initialized at $t = 0$ by the initial guess \tilde{u}_0^{init} for \tilde{u}_0 and \tilde{v}_0 .

The prediction of the wave field u_r at the sensor plane corresponding to the r th phase-mask is calculated using FFT (Step 1).

Step 2 corresponds to solution of the problem (23). The estimate $u_r^{t+1}[k]$ is calculated from minimization of \mathcal{L}_1 with respect to u_r provided given values of $o_r[k]$ and $u_r^{t+1/2}[k]$. The formulas (48)-(50) defining the operator $\mathcal{G}(o_r[k], u_r^{t+1/2}[k])$ in Step 2 are given in Appendix II.

Step 3 corresponds to solution of the problem (23) with minimization of \mathcal{L}_1 with respect to \tilde{u}_0 . These calculations are produced in the FFT domain.

The $\Phi_a \cdot \text{mod}(\tilde{\mathbf{u}}_0^{t+1})$ and $\Phi_\varphi \cdot \text{angle}(\tilde{\mathbf{u}}_0^{t+1})$ are the vectors of the spectrum representations for amplitude and phase, respectively. Steps 4 and 5 mean the filtering of these spectra using the thresholding operations $\mathfrak{Th}_{\tau_a \gamma_a}$ and $\mathfrak{Th}_{\tau_\varphi \gamma_\varphi}$. The formulas (57)-(58) for the thresholding operations are derived in Appendix II as the solution of the problem (24). The estimates of the amplitude

$\boldsymbol{\theta}_a^{t+1}$ and phase $\boldsymbol{\theta}_\varphi^{t+1}$ spectra are used for calculation of $\tilde{\mathbf{v}}_0^{t+1}$ in Step 6 according to the formula (15). FFT of this estimate reshaped in the image \tilde{v}_0^{t+1} , $\tilde{V}_0^t = \mathcal{F}\mathcal{F}\mathcal{T}\{\tilde{v}_0^t\}$, is used in Step 3 for calculation of the update for the object distribution.

We use the name 4f-SPAR for the developed algorithm as the abbreviation for **S**parse **P**hase-**A**mplitude **R**econstruction with "4f" added in order to emphasize that the algorithm is developed for the optical **4f** system.

The initial guess \tilde{u}_0^{init} for (28) is calculated according to the ‘*no filtering*’ option of the 4f-SPAR algorithm. It is a simplified version 4f-SPAR obtain by dropping the filtering stages (32)-(34) and assuming that $V_0^t = \tilde{U}_0^t$.

This ‘*no filtering*’ algorithm is similar but not identical to the Augmented Lagrangian (AL) algorithm developed for the phase retrieval in [40], where the linear equation-constraints (17) are treated using the Lagrange multipliers.

6. Algorithm implementation and complexity

The analysis and synthesis frames are designed only ones for phase and amplitude of the initialization \tilde{u}_0^{init} at the stage (27) of the algorithm. After that they are fixed through the iterations. To build the BM3D groups, we use the block-matching procedure from [33].

In order to simplify the developed algorithm the solution (52) derived for noiseless data is used for both noiseless and noisy data. Then, Step 2 of the algorithm is of the form

$$u_r^{t+1}[k] = \frac{u_r^{t+1/2}[k]}{|u_r^{t+1/2}[k]|} \sqrt{o_r[k]}. \quad (35)$$

This replacement of the module of $u_r^{t+1/2}[k]$ by the square root of the observed intensity is the standard stage of the GSF techniques. In particular, it is used for the phase retrieval from multiple observations in the SBMIR algorithm (see [4], [5], [11], [16]).

In our paper this replacement is obtained as an optimal solution for the problem (23) provided that the intensity observations are treated as accurate noiseless. Using this solution for the noisy data we assume that the corresponding inaccuracy is compensated by the powerful filtering of the spectra at Steps 4 and 5 of the algorithm.

Most calculations of the 4f-SPAR algorithm are based on FFT. We use the double-size computational support-window $2N_1 \times 2N_2$ for the object u_0 , images u_r and \tilde{M}_r . It assumes zero-padding of u_0 . For the image plane it means reconstruction of the u_r for the double-size support area, i.e. extension of the wave field reconstruction outside the sensor. Details of this double-size FFT

technique can be seen in [38] and in Section 5 of [37].

20-50 iterations of the ‘*no filtering*’ algorithm are sufficient in order to get a good quality \tilde{u}_0^{init} for 4f-SPAR. Note that this initialization algorithm is much faster than 4f-SPAR because the analysis and synthesis frames are not used and the spectra θ_φ , θ_a are not calculated.

The computational complexity of the algorithm is characterized by the time required for 100 iterations, including the initialization iterations. For an image 256×256 it takes about 150 sec for the computer and the software used in the experiments: Intel Core 2Duo E8400 @ 3GHz, RAM 4GB, Windows Xp SP3, Matlab 7.9.0 (R2009b).

Following the principle of the reproducible research [42] we make our MATLAB programs for the demo version of 4f-SPAR publicly available for testing: <http://www.cs.tut.fi/~lasip/DDT/>.

7. Simulation experiments

We discuss two groups of experiments. In the first group, the SLM phase mask imitates the multiple plane phase retrieval with various distances between the object and image planes. In the second group, the efficiency of the random phase modulation is demonstrated.

We consider the object wave fields with the amplitude and/or phase modulation in the form $u_0[k] = |u_0[k]| \cdot \exp(j \cdot \varphi_0[k])$. For the amplitude modulation $\varphi_0[k] \equiv 0$, $\text{abs}(u_0[k]) = w[k] + .2$. For the phase modulation $\text{abs}(u_0[k]) \equiv 1$, $\varphi_0[k] = \pi(w[k] - 1/2)/5$. Here $w[k]$, $0 \leq w[k] \leq 1$, is a spatially varying test-image. The results are shown for square (256×256) test-images: binary *chessboard* and gray-scale *Lena*.

Pixelated models for the object and sensor planes have square pixels $\Delta_x \times \Delta_x$ with $\Delta_x = 3.45 \mu m$ and 100% fill factors. The pixels of SLM are square $\Delta_v \times \Delta_v$ with $\Delta_v = 8.0 \mu m$. The wavelength $\lambda = .532 \mu m$ corresponds to a green laser.

Observations are generated using the formulas (9) and (10) where the noise standard deviation $\sigma = 0.05$. The double-size FFT technique mentioned in the previous section is exploited for these calculations in order to obtain realistic observations including diffraction effects. The in-focus distance for these double size images is calculated as $f = 2N_1 \cdot \Delta_x \Delta_v / \lambda$, for $N_1 = 256$ it gives $f = 26.58 mm$.

The following four parameters are used in order to tune the algorithm: γ ($\gamma_r = \gamma$, $r = 1, \dots, K$), γ_0 , $\tau_a \gamma_a$ and $\tau_\varphi \gamma_\varphi$. Overall, large values of the

threshold parameters $\tau_a\gamma_a$, $\tau_\varphi\gamma_\varphi$ and smaller values of γ_0 result in a stronger filtering of both phase and amplitude.

The following values of these parameters are found experimentally and well fit to our experiments with the test-images used for phase and amplitude modulation: $\gamma = 1$, $\tau_a\gamma_a = 0.04$, $\tau_\varphi\gamma_\varphi = 0.04$. The parameter γ_0 is different for different types of the test-images. For gray-scale Lena $\gamma_0 = 1/5$, and for piece-wise invariant chessboard $\gamma_0 = 1/10$.

7.A. Multiple plane phase diversity

In the work by Falldorf, et al. [11] the optical mask $M_r[l]$ (SLM) is used as a phasor in the Fourier plane imitating a wave field propagation for various distances. The complex transmittance of the phase mask is calculated using the formula (7) from [11],

$$\tilde{M}_r[l_1, l_2] = \exp(2\pi j \cdot z_r \sqrt{1 - \Delta_v^2(l_1^2 + l_2^2)/f^2/\lambda}), \quad (36)$$

where the distance between the object and sensor planes is $z_r = z_1 + r\Delta_z$, $r = 0, \dots, K - 1$.

In our simulation experiments we follow this scenario and use this phase mask. It is found by simulation that a proper selection of the parameters z_1 , K and Δ_z for (36) is important for accurate reconstruction of phase and

amplitude. Further results are given assuming that $z_1 = f$, $K = 10$ and $\Delta_z = 20 \text{ mm}$.

In order to evaluate the efficiency of the developed phase/amplitude regularization (filtering) the 4f-SPAR algorithm is compared versus the ‘*no filtering*’ and SBMIR algorithms. Recall that the former is of the same structure as 4f-SPAR but with no phase and amplitude filtering.

In Fig. 2-3 the reconstructions of phase and amplitude are shown for the ‘*no filtering*’ algorithm. The noise components as well as wiggles typical for the optical diffractions are seen, in particular, in the chessboard reconstructions in Fig. 2. The reconstructions in Fig. 4-5 are obtained for the same observations by 4f-SPAR using the phase/amplitude filtering. The accuracy of the reconstructions is characterized by the root-mean-squared-error (RMSE) criterion calculated independently for phase and amplitude. The corresponding values of RMSE are shown in the figures.

The visual advantage of the 4f-SPAR reconstruction is quite obvious. The noise and wiggle effects are nearly eliminated and sharp and clear images are obtained in the reconstructions.

The phase from the intensity measurements can be reconstructed up to an

arbitrary additive constant. In order to take off this ambiguity, *RMSE* for the object phase is calculated for $\phi_0 - \hat{\phi}_0 - \text{mean}(\phi_0 - \hat{\phi}_0)$, where ϕ_0 is the true phase, $\hat{\phi}_0$ is an estimate of the phase, and $\text{mean}(\phi_0 - \hat{\phi}_0)$ stands for the mean value of the estimation error calculated over the image.

In more details the accuracy of 4f-SPAR is demonstrated in Table 1, where the results obtained using the SBMIR and ‘*no filtering*’ algorithms are shown.

The advantage of 4f-SPAR is obvious, in particular for the binary chess-board test-image. For the reconstruction of phase for the phase object and for reconstruction of amplitude for the amplitude object RMSE values are about two/four times lower for 4f-SPAR algorithm as compared with the ‘*no filtering*’ algorithm. For the phase object SBMIR fails to reconstruct phase giving the divergence after 30 iterations. For the amplitude object and amplitude reconstruction SBMIR converges with RMSE=.075 after 100 iterations. This RMSE value is about twice larger than RMSE achieved by the algorithm with ‘*no filtering*’ and about 8 times larger of RMSE for 4f-SPAR.

For the gray-scale test-image Lena, the numerical advantage in RMSE values of 4f-SPAR is not so impressive. However, visually the superiority of 4f-SPAR is obvious if we compare images in Fig.3 with the images in Fig.5.

We do not show the images obtained by SBMIR because they are much worse than those obtained by the ‘*no-filtering*’ algorithm.

7.B. Random phase modulation

One of the alternative ways to get a stronger wave field modulation than it can be achieved in the multiple plane scenario is using the masks with a random phase distribution. This sort of the random masks become quite popular in many applications, see for instance [27] and [39].

Let the phase masks \tilde{M}_r be random and generated in the form:

$$\tilde{M}_r[l_1, l_2] = \exp(2\pi j\psi_r[l_1, l_2]), \quad r = 1, \dots, K, \quad (37)$$

with an independent random phase $\psi_r[l_1, l_2]$ uniformly distributed over the interval $[0, \varkappa)$, $0 < \varkappa \leq 1$.

The parameter \varkappa defines the depth of the phase modulation, with its maximum value $\varkappa = 1$, giving the random phase uniformly distributed over the entire period $[0, 2\pi)$.

In the signal domain the discrete convolution

$$u_r = \tilde{u}_0 \otimes \tilde{m}_r \quad (38)$$

corresponds to the forward propagation model (9) given in the Fourier do-

main.

In Eq. (38), $\tilde{u}_0 = \mathcal{F}\mathcal{F}\mathcal{T}^{-1}\{\tilde{U}_0\}$ and $\tilde{m}_r = \mathcal{F}\mathcal{F}\mathcal{T}^{-1}\{\tilde{M}_r\}$, and \otimes stands for the 2D discrete circular convolution.

In Fig. 6 we show the 1D cross-sections of $\text{abs}^2(\tilde{m}_r[k_1, k_2])$ for $\varkappa = 1, 0.99, 0.95, 0.5$. These cross-sections are centered with respect to $k_1 = k_2 = 0$.

We can note that for $\varkappa < 1$, these cross-sections have a similar structure: a sharp strong peak at the center and a low level wide floor covering more or less uniformly the whole support of the function. For smaller \varkappa the relative height of this floor becomes essentially lower. For $\varkappa = 1$ the peak disappears, and the floor becomes higher and dominates the distribution of $\text{abs}^2(\tilde{m}_r[k_1, k_2])$. It can be seen from Eq. (38) that this structure of \tilde{m}_r results in translation of the power of \tilde{u}_0 out of the signal support interval. A higher level of the floor in $\text{abs}^2(\tilde{m}_r[k_1, k_2])$ means that a more power of \tilde{u}_0 appears out of the support of u_r , i.e. out of the sensor recording data. Thus, for higher values of \varkappa more power of \tilde{u}_0 cannot be registered by the sensor. The maximum of this disturbance in data registration is achieved at $\varkappa = 1$.

In the same time, very small values of \varkappa mean, that there is no phase modulation, the registered images are not different and the wave field cannot

be reconstructed. In the limit $\lim_{\varkappa \rightarrow 0} \tilde{m}_r[k_1, k_2] = \delta_{k_1} \delta_{k_2}$. From this behavior for $\varkappa \rightarrow 0$ and $\varkappa \rightarrow 1$ follows, that there is an optimal intermediate value of \varkappa enabling the best wave field reconstruction. We do not discuss a random phase optimization in this paper. In what follows we use $\varkappa = .5$, which is not optimal but gives good results for all experiments.

In Table 2 we show RMSE values obtained for the experiments considered in Table 1 with the only difference that the multiple plane phase modulation is replaced by the random phase modulation. Comparison of the corresponding RMSE values in Tables 1 and 2 is in favor of the random phase modulation for all cases. As an another advantage of the random phase modulation we wish to mention about a twice faster convergence of the algorithm.

8. Conclusion

The developed 4f-SPAR algorithm demonstrates a good accuracy and a high quality imaging for phase and amplitude reconstructions in the 4f optical setup. The artifacts typically appeared in the conventional techniques are nearly eliminated by 4f-SPAR. Three components of the proposed approach enable the advance performance of the algorithm. First, the image modeling and the regularization are separate for phase and amplitude. Second, the

BM3D-frames used in our algorithm implementation provide rich and over-complete sets of functions for sparse approximations of phase and amplitude. Third, instead of a single objective function typical for the conventional CS techniques we use a vector optimization with two objective functions. The algorithm searches for a fixed-point giving a balance between two quality measures defined by these objective functions. This vector optimization decouples the inversion and the filtering operations and results in the iterative algorithm simple in implementation and highly efficient.

Appendix I

Proof of (7)

Let us start from some auxiliary results. First of all note that $\sum_{k_1=0}^{N_1-1} e^{-j2\pi\frac{k_1 l_1}{N_1}}$ is a periodic function of l_1 with the period equal to N_1 . Then,

$$\frac{1}{N_1} \sum_{k_1=0}^{N_1-1} e^{-j2\pi\frac{k_1 l_1}{N_1}} = \delta_{l_1+N_1\eta_1}, \quad (39)$$

where $\delta_{l_1+N_1\eta_1}$ is the Kronecker's symbol, $\delta_{l_1+N_1\eta_1} = 1$ for $l_1 + N_1\eta_1 = 0$ and $\delta_{l_1} = 0$ otherwise; η_1 is an arbitrary integer. Calculating FFT for $U_0[l_1, l_2]$ and using Eq. (39) we obtain

$$\begin{aligned} \mathcal{FFT}_{l_1, l_2}\{U_0[l_1, l_2]\}[k_1, k_2] &= \sum_{l_1=0}^{N_1-1} \sum_{l_2=0}^{N_2-1} U_0[l_1, l_2] e^{-j2\pi(\frac{k_1 l_1}{N_1} + \frac{k_2 l_2}{N_2})} = \\ & \sum_{k'_1=0}^{N_1-1} \sum_{k'_2=0}^{N_2-1} u_0[k'_1, k'_2] \sum_{l_1=0}^{N_1-1} \sum_{l_2=0}^{N_2-1} e^{-j2\pi(\frac{(k_1+k'_1)l_1}{N_1} + \frac{(k_2+k'_2)l_2}{N_2})} = \\ & N_1 N_2 \sum_{k'_1=0}^{N_1-1} \sum_{k'_2=0}^{N_2-1} u_0[k'_1, k'_2] \cdot \delta_{k_1+k'_1+N_1\eta_1} \cdot \delta_{k_2+k'_2+N_2\eta_2}, \end{aligned} \quad (40)$$

where η_1, η_2 are arbitrary integers.

We use Eq. (40) provided that both k_1, k_2 and k'_1, k'_2 simultaneous belong to the intervals $0 \leq k_1, k'_1 \leq N_1 - 1$, $0 \leq k_2, k'_2 \leq N_2 - 1$. Nonzero values for $\mathcal{FFT}_{l_1, l_2}\{U_0[l_1, l_2]\}[k_1, k_2]$ can be obtained only if $\eta_1 = \eta_2 = -1$, then it

follows from (40) that

$$\mathcal{F}\mathcal{F}\mathcal{T}_{l_1, l_2}\{U_0[l_1, l_2]\}[k_1, k_2] = u_0[N_1 - k_1, N_2 - k_2], \quad (41)$$

$$0 \leq k_1 \leq N_1 - 1, 0 \leq k_2 \leq N_2 - 1.$$

Recall, that $u_0[N_1, N_2 - k_2] = u_0[0, N_2 - k_2]$ and $u_0[N_1 - k_1, N_2] = u_0[N_1 - k_1, 0]$.

Now, let us prove Eq. (7). A discrete version of the integral formula (1) can be given in the form

$$c(l_1\Delta_{v_1}, l_2\Delta_{v_2}) = \frac{1}{j\lambda f} \sum_{k_1=0}^{N_1-1} \sum_{k_2=0}^{N_2-1} u_0(k_1\Delta_{x_1}, k_2\Delta_{x_2}) e^{-j2\pi(k_1\Delta_{x_1} \cdot \frac{l_1\Delta_{v_1}}{\lambda f} + k_2\Delta_{x_2} \cdot \frac{l_2\Delta_{v_2}}{\lambda f})} \Delta_{x_1} \Delta_{x_2}. \quad (42)$$

Provided the conditions (6) it gives

$$c[l_1, l_2] = \frac{\Delta_{x_1} \Delta_{x_2}}{j\lambda f} \mathcal{F}\mathcal{F}\mathcal{T}\{u_0[k_1, k_2]\} = \frac{\Delta_{x_1} \Delta_{x_2}}{j\lambda f} U_0[l_1, l_2]. \quad (43)$$

Thus, in the discrete version of Eq. (1) there is no scaling of the arguments provided (6).

Due to Eqs. (2) and (43) the discrete model for $u_r(k_1\Delta_{x_1}, k_2\Delta_{x_2})$ is of the form

$$u_r[k_1, k_2] = \frac{\Delta_{v_1} \Delta_{v_2}}{j\lambda f} \mathcal{F}\mathcal{F}\mathcal{T}\{c[l_1, l_2] \cdot M_r[l_1, l_2]\}. \quad (44)$$

Calculating FFT for $u_r[k_1, k_2]$ and using Eq. (41) we found that

$$U_r[l_1, l_2] = \mathcal{FFT}_{k_1, k_2}\{u_r[k_1, k_2]\}[l_1, l_2] = \quad (45)$$

$$\frac{N_1 N_2 \Delta_{v_1} \Delta_{v_2}}{j\lambda f} c[-l_1 + N_1, -l_2 + N_2] \cdot M_r[-l + N_1, -l_2 + N_2].$$

Finally, inserting Eq. (43) in this formula and again using Eq. (6) we obtain

$$U_r[l_1, l_2] = \frac{N_1 N_2 \Delta_{v_1} \Delta_{v_2}}{j\lambda f} \cdot \frac{\Delta_{x_1} \Delta_{x_2}}{j\lambda f} \times$$

$$U_0[-l_1 + N_1, -l_2 + N_2] \cdot M_r[-l_1 + N_1, -l_2 + N_2] =$$

$$-U_0[-l_1 + N_1, -l_2 + N_2] \cdot M_r[-l_1 + N_1, -l_2 + N_2].$$

It completes the proof of Eq. (7).

Appendix II

Derivation of the algorithm

Minimization of \mathcal{L}_1 on u_r (Problem (23)). The objective function \mathcal{L}_1 (18) is additive with respect to $u_r[k]$. Thus, minimization can be produced separately for every r and k . These calculations similar to used in [40] give the minimum condition in the form

$$\begin{aligned} \partial\mathcal{L}_1/\partial u_r^*[k] &= \frac{1}{\sigma_r^2}(|u_r[k]|^2 - o_r[k]) \cdot u_r[k] + \\ &\frac{1}{\gamma_r}(u_r[k] - z_r[k]) = 0, \end{aligned} \quad (46)$$

where we use notation $z_r[k] \triangleq \mathcal{F}\mathcal{F}\mathcal{T}^{-1}\{\tilde{U}_0[l]\tilde{M}_r[l]\}[k]$.

It follows

$$u_r[k] = \frac{z_r[k]}{(|u_r[k]|^2 - o_r[k]) \cdot \frac{\gamma_r}{\sigma_r^2} + 1}. \quad (47)$$

Then for the modulus we have

$$|u_r[k]| = \frac{|z_r[k]|}{(|u_r[k]|^2 - o_r[k]) \cdot \frac{\gamma_r}{\sigma_r^2} + 1}. \quad (48)$$

The last equation may have a single or three real solutions. We are looking for a nonnegative one for $|u_r[k]|$. Let us denote this nonnegative solution for Eq. (48) as $|\bar{u}_r[k]|$, then the corresponding complex-valued $u_r[k]$ is calculated

from Eq. (47) as

$$u_r[k] = \frac{z_r[k]}{(|\bar{u}_r[k]|^2 - o_r[k]) \cdot \frac{\gamma_r}{\sigma_r^2} + 1}. \quad (49)$$

For brevity we denote the nonlinear operator giving the solution (49) as

$$u_r[k] = \mathcal{G}(o_r[k], z_r[k]). \quad (50)$$

This estimate of $u_r[k]$ is calculated separately for each k and r from the observed intensity $o_r[k]$ and the prediction $z_r[k]$ for $u_r[k]$ obtained from u_0 as $z_r[k] \triangleq \mathcal{F}_l^{-1}\{M_r[l]\tilde{U}_0[l]\}[k]$.

Let us consider the noiseless observations as a special case of the problem.

Assuming that $\sigma_r^2/\gamma_r \rightarrow 0$ we obtain from Eq. (48) that

$$(|\bar{u}_r[k]|^2 - o_r[k]) + \sigma_r^2/\gamma_r \cdot |\bar{u}_r[k]| = |z_r[k]| \cdot (\sigma_r^2/\gamma_r). \quad (51)$$

It follows that $|\bar{u}_r[k]|^2 - o_r[k] \rightarrow 0$.

Let us rewrite Eq. (49) in the form

$$u_r[k] = \frac{z_r[k]}{|z_r[k]|} \frac{|z_r[k]| \sigma_r^2/\gamma_r}{|\bar{u}_r[k]|^2 - o_r[k] + \sigma_r^2/\gamma_r}.$$

Inserting in this equations (51) we find

$$u_r[k] \rightarrow \frac{z_r[k]}{|z_r[k]|} |\bar{u}_r[k]| = \frac{z_r[k]}{|z_r[k]|} \sqrt{o_r[k]}.$$

It is proved that in the noiseless case the solution of the problem (23) is of the form

$$u_r[k] = \frac{z_r[k]}{|z_r[k]|} \sqrt{o_r[k]}. \quad (52)$$

It means that $u_r[k]$ has the module equal to $\sqrt{o_r[k]}$, and the phase equal to the phase of $z_r[k]$.

Minimization of \mathcal{L}_1 on u_0 (Problem (23)).

The part of \mathcal{L}_1 (18) depending on u_0 is $\mathcal{L}'_1 = \sum_{r=1}^K \frac{1}{\gamma_r} \sum_k |u_r[k] - \mathcal{F}\mathcal{F}\mathcal{T}^{-1}\{\tilde{M}_r[l]\tilde{U}_0[l]\}|^2 + \frac{1}{\gamma_0} \|\tilde{\mathbf{u}}_0 - \tilde{\mathbf{v}}_0\|_2^2$.

Let us calculate \mathcal{L}'_1 in the frequency domain using FFT of the corresponding Fourier domain variables. According to the Parseval equation: $\sum_k a[k]b^*[k] = \frac{1}{n} \sum_l A[l]B^*[l]$, where $A[l]$, $B[l]$ are FFT of vectors $a[k]$ and $b[k]$, and n is a length of $a[k]$, $b[k]$.

It follows that

$$\mathcal{L}'_1 = \sum_r \frac{1}{\gamma_r n} \sum_l |U_r[l] - \tilde{M}_r[l] \cdot \tilde{U}_0[l]|^2 + \frac{1}{\gamma_0 n} \sum_l |\tilde{U}_0[l] - \tilde{V}_0[l]|^2 \quad (53)$$

Minimization on $\tilde{U}_0[l]$ produced in the FFT domain gives the minimum condition in the form $\partial\mathcal{L}'_1/\partial\tilde{U}_0^*[l] = 0$.

After some manipulation we obtain

$$\partial \mathcal{L}'_1 / \partial \tilde{U}_0^*[l] = \sum_r \frac{1}{\gamma_r n} (U_r[l] - \tilde{M}_r[l] \cdot \tilde{U}_0[l]) \tilde{M}_r^*[l] + \frac{1}{\gamma_0 n} (\tilde{U}_0[l] - \tilde{V}_0[l]) = 0,$$

and further the solution is of the form

$$\tilde{U}_0[l] = \frac{\sum_r \frac{1}{\gamma_r} U_r[l] \tilde{M}_r^*[l] + \frac{1}{\gamma_0} \tilde{V}_0[l]}{\sum_r \frac{1}{\gamma_r} + \frac{1}{\gamma_0}}. \quad (54)$$

It is used in these calculations that for the phase mask $|\tilde{M}_r[l]|^2 = 1$.

Minimization of \mathcal{L}_2 on $\boldsymbol{\theta}$ (Problem (24)).

Let us consider the optimization problem

$$\min_{\boldsymbol{\theta}} \tau \cdot \|\boldsymbol{\theta}\|_{l_p} + \frac{1}{2} \|\boldsymbol{\theta} - \mathbf{B}\|_2^2, \quad (55)$$

where $\boldsymbol{\theta} \in \mathbb{R}^m$ and $\mathbf{B} \in \mathbb{R}^m$ are vectors, and l_p -norm can be $\|\boldsymbol{\theta}\|_0$ or $\|\boldsymbol{\theta}\|_1$.

Due to the additive nature of the norms the problem (55) can be solved independently for each component $\boldsymbol{\theta}_i$ of the vector $\boldsymbol{\theta}$:

$$\boldsymbol{\theta}_i = \arg \min_{\boldsymbol{\theta}_i} \tau \cdot \|\boldsymbol{\theta}_i\|_{l_p} + \frac{1}{2} (\boldsymbol{\theta}_i - \mathbf{B}_i)^2. \quad (56)$$

There is an analytical solution for (56) known as the hard- and soft thresholding (or hard- and soft shrinkage) operators, respectively for l_0 and l_1 .

Let us denote this operator as

$$\boldsymbol{\theta} = \mathfrak{Th}_\tau(\mathbf{B}), \quad (57)$$

where \mathbf{B} is an input-vector and $\boldsymbol{\theta}$ is a solution-vector returned by the operator.

For l_0 and l_1 this elementwise operator is specified as (e.g. [31])

$$\boldsymbol{\theta} = \mathfrak{Th}_\tau(\mathbf{B}) = \tag{58}$$

$$\begin{cases} \mathfrak{Th}_\tau^{soft}(\mathbf{B}) = \text{sign}(\mathbf{B}) \circ \max(|\mathbf{B}| - \tau, 0), & \text{if } l_p = l_1, \\ \mathfrak{Th}_{\sqrt{2\tau}}^{hard}(\mathbf{B}) = \mathbf{B} \circ 1(|\mathbf{B}| \geq \sqrt{2\tau}), & \text{if } l_p = l_0, \end{cases}$$

where the indexes '*soft*' and '*hard*' indicate the type of the solution.

The threshold parameters for the soft- and hard thresholdings are different.

The solutions for the problem (24) are obtained from Eq. (58) and are corresponding to the minimization of $\tau_a \cdot \|\boldsymbol{\theta}_a\|_{l_p} + \frac{1}{2\gamma_a} \|\boldsymbol{\theta}_a - \Phi_a \text{mod}(\mathbf{u}_0)\|^2$ with respect to $\boldsymbol{\theta}_a$ and the minimization of $\tau_\varphi \cdot \|\boldsymbol{\theta}_\varphi\|_{l_p} + \frac{1}{2\gamma_\varphi} \|\boldsymbol{\theta}_\varphi - \Phi_\varphi \text{arg}(\mathbf{u}_0)\|^2$ with respect to $\boldsymbol{\theta}_\varphi$, respectively.

A. Acknowledgments

This work was supported by the Academy of Finland: project no. 213462, 2006-2011 (Finnish Programme for Centres of Excellence in Research) and project no. 138207, 2011-2014. The authors want to thank the anonymous reviewers for their constructive comments and suggestions.

References

1. D. L. Misell, "An examination of an iterative method for the solution of the phase problem in optics and electron optics: I. Test calculations," *J. Phys. D Appl. Phys.* 6(18), 2200–2216 (1973).
2. W. O. Saxton, "Correction of artefacts in linear and nonlinear high resolution electron micrographs," *J. Microsc. Spectrosc. Electron.* 5, 661–670 (1980).
3. G. Pedrini, W. Osten, and Y. Zhang, "Wave-front reconstruction from a sequence of interferograms recorded at different planes," *Opt. Lett.* vol.30, pp. 833-835 (2005).
4. P. Almero, G. Pedrini and W. Osten, "Complete wavefront reconstruction using sequential intensity measurements of a volume speckle field," *Appl. Opt.*, vol. 45, pp.8596-8605 (2006).
5. P. Almero, A. M. S. Maallo, and S. Hanson, "Fast-convergent algorithm for speckle-based phase retrieval and a design for dynamic wavefront sensing," *Appl. Opt.* 48, pp.1485-1493 (2009).
6. C. Kohler, F. Zhang, and W. Osten, "Characterization of a spatial light modulator and

- its application in phase retrieval,” *Appl. Opt.* 48(20), 4003–4008 (2009).
7. L. Camacho, V. Micy, Z. Zalevsky, and J. Garcha, “Quantitative phase microscopy using defocusing by means of a spatial light modulator,” *Opt. Express* 18(7), 6755–6766 (2010).
 8. J. M. Rodenburg, and H. M. L. Faulkner, “A phase retrieval algorithm for shifting illumination,” *Appl. Phys. Lett.* 85(20), 4795–4797 (2004).
 9. G. R. Brady, M. Guizar-Sicairos, and J. R. Fienup, “Optical wavefront measurement using phase retrieval with transverse translation diversity,” *Opt. Express* 17(2), 624–639 (2009).
 10. J. Glückstad, and D. Palima, “*Generalised phase contrast: applications in optics and photonics*,” Springer Series in Optical Sciences, vol. 146 (Springer 2009).
 11. C. Falldorf, M. Agour, C. v. Kopylow, and R. B. Bergmann, “Phase retrieval by means of a spatial light modulator in the Fourier domain of an imaging system,” *Appl. Opt.* 49(10), pp. 1826–1830 (2010).
 12. R. W. Gerchberg and W. O. Saxton, A practical algorithm for the determination of phase from image and diffraction plane pictures, *Optik*, 35, pp. 237–246 (1972).
 13. J. R. Fienup, Phase retrieval algorithms: a comparison, *Appl. Opt.*, 21, pp. 2758–2769 (1982).
 14. G. Yang, B. Dong, B. Gu, J. Zhuang, and O. K. Ersoy, “Gerchberg-Saxton and Yang-Gu algorithms for phase retrieval in a nonunitary transform system: a comparison,” *Appl. Opt.* 33, pp. 209–218 (1994).
 15. V. Y. Ivanov, V. P. Sivokon, and M. A. Vorontsov, “Phase retrieval from a set of intensity measurements: theory and experiment,” *JOSA A* 9, pp. 1515–1524 (1992).

16. G. Pedrini, W. Osten, and Y. Zhang, "Wave-front reconstruction from a sequence of interferograms recorded at different planes," *Opt. Lett.* **30**, pp. 833–835 (2005).
17. J.R. Fienup, "Phase-Retrieval Algorithms for a Complicated Optical System," *Appl. Opt.* **32**, pp. 1737-1746 (1993).
18. R. Irwan and R.G. Lane, "Phase retrieval with prior information," *JOSA A* vol. 15, no. 9 66, pp. 2302-2311 (1998).
19. R.G. Lane, "Phase Retrieval Using Conjugate Gradient Minimization," *J. Modern Optics* **38**, pp. 1797-1813 (1991).
20. E. J. Candes, J. Romberg, and T. Tao, "Robust uncertainty principles: exact signal reconstruction from highly incomplete frequency information," *IEEE Trans. Inf. Theory* **52**, 489–509 (2006).
21. E. J. Candes and T. Tao, "Near-optimal signal recovery from random projections: universal encoding strategies" *IEEE Trans. Inf. Theory* **52**, 5406–5425 (2006).
22. D. L. Donoho, "Compressed sensing," *IEEE Trans. Inf. Theory* **52**, 1289–1306 (2006).
23. S. Gazit, A. Szameit, Y. C. Eldar, M. Segev, "Super-resolution and reconstruction of sparse sub-wavelength images, " *Optics Express* **17**, pp. 23920-23946 (2009).
24. D. J. Brady, K. Choi, D. L. Marks, R. Horisaki and S. Lim, "Compressive holography," *Optics Express*, **17**, pp. 13040-13049 (2009).
25. C. F. Cull, D. A. Wikner, J. N. Mait, M. Mattheiss, and D. J. Brady, "Millimeter-wave compressive holography," *Applied Optics*, **49**, pp. 67-82 (2010).
26. K. Choi, R. Horisaki, J. Hahn, S. Lim, D.L.Marks, T.J. Schulz, D.J. Brady, "Compressive holography of diffuse objects," *Applied Optics* **49**, pp. H1-H10 (2010).

27. Y. Rivenson, A. Stern, B. Javidi, "Compressive Fresnel holography," *Journal of Display Technology* **6**, pp. 506-509 (2010).
28. Z. Xu and E. Y. Lam, "Image reconstruction using spectroscopic and hyperspectral information for compressive terahertz imaging," *J. Opt. Soc. Am. A* **27**, 1638-1646 (2010).
29. J. W. Goodman, *Introduction to Fourier optics*, 3rd Ed. (Roberts & Company, Englewood, 2005).
30. D. Han, K. Kornelson, D. Larson, E. Weber, *Frames for Undergraduates* (Student Mathematical Library, AMS, 2007).
31. M. Elad, *Sparse and Redundant Representations: From Theory to Applications in Signal and Image Processing*, Springer, 2010.
32. J.-L. Starck, F. Murtagh, J. Fadili, *Sparse Image and Signal Processing: Wavelets, Curvelets, Morphological Diversity*, Cambridge University Press, 2010.
33. K. Dabov, A. Foi, V. Katkovnik, and Egiazarian, K., "Image denoising by sparse 3D transform-domain collaborative filtering," *IEEE Transactions on Image Processing*, vol. **16**, pp. 2080 - 2095 (2007).
34. Katkovnik, V., A. Foi, K. Egiazarian, and J. Astola, "From local kernel to nonlocal multiple-model image denoising", *Int. J. Computer Vision*, vol. 86, no. 1, pp. 1-32 (2010).
35. A. Danielyan, V. Katkovnik and K. Egiazarian, "Image deblurring by augmented Lagrangian with BM3D frame prior," *Workshop on Information Theoretic Methods in Science and Engineering (WITMSE)* (2010).
36. V. Katkovnik, A. Danielyan and K. Egiazarian, "Decoupled inverse and denoising for image deblurring: variational BM3D-frame technique," *IEEE International Conference*

- on Image Processing (ICIP)* (2011).
37. Katkovnik, V. and J. Astola, "High-accuracy wave field reconstruction: decoupled inverse imaging with sparse modeling of phase and amplitude," *JOSA A* (2011).
 38. V. Katkovnik, J. Astola, and K. Egiazarian, "Discrete diffraction transform for propagation, reconstruction, and design of wave field distributions," *Appl. Opt.* **47**, pp. 3481-3493 (2008).
 39. B. Javidi, G. Zhang, and J. Li, "Encrypted optical memory using double-random phase encoding," *Appl. Opt.* **36**(5), pp. 1054–1058 (1997).
 40. A. Migukin, Katkovnik, V. and Astola, J., "Wave field reconstruction from multiple plane intensity-only data: Augmented Lagrangian algorithm", *JOSA A*, **28**, pp.993-1002 (2011).
 41. D. P. Bertsekas, *Nonlinear Programming* (Second ed., Cambridge, MA.: Athena Scientific, 1999).
 42. J. B. Buckheit and D. L. Donoho, "WaveLab and reproducible research," Dept. of Statistics, Stanford University, Tech. Rep. 474 (1995), http://www-stat.stanford.edu/~wavelab/Wavelab_850/wavelab.pdf.

List of Figure Captions

Fig.1 4f optical system: object, Fourier and image planes are in-focus of two lenses, optical mask (SLM) in Fourier focus plane of first lens.

Fig.2 The amplitude modulation object with the binary phase (chessboard test-image). The reconstruction by the ‘*no filtering*’ algorithm without phase/amplitude filtering. In the cross-sections thick (‘red’ in color) and thin (‘blue’ in color) lines show the true signal and the reconstructions, respectively. RMSE values for the phase and amplitude are shown at the top. The visual quality of the reconstruction is quite poor: noise, wiggles, waves, etc. are clearly seen.

Fig.3 The phase modulation object with the Lena test-image. The reconstruction by the “*no filtering*” algorithm without phase/amplitude filtering. The visual quality of the reconstruction is quite poor: noise, wiggles, waves, etc. are clearly seen.

Fig.4 The amplitude modulation object with the binary phase (chessboard test-image). The reconstruction by the 4f-SPAR algorithm. The visual quality of the reconstruction is very good, noise and diffraction artifacts are wiped out. Compare with Fig. 2, where the filtering is not used.

Fig.5 The phase modulation object with the Lena test-image. The reconstruction by the 4f-SPAR algorithm. The visual quality of the reconstruction is very good, in particular versus Fig.3, where the filtering is not used.

Fig.6 Cross-sections of $\text{abs}^2(\tilde{m}_r[k_1, k_2])$ for $\varkappa = 1, 0.99, 0.95, 0.5$.

List of Table Captions

Table 1. RMSE values for amplitude and phase reconstructions. Comparison of 4f-SPAR versus the ‘*no filtering*’ and SBMIR algorithms. The test-images chessboard and Lena are used for the phase and amplitude modulation. The phase mask imitates the multiple plane phase retrieval scenario.

Table 2. RMSE values for amplitude and phase reconstructions. Comparison of 4f-SPAR versus the ‘*no filtering*’ and SBMIR algorithms. The test-images chessboard and Lena are used for the phase and amplitude modulation. The random phase mask is used for the wave field modulation.

Table 1. RMSE values for amplitude and phase reconstructions. Comparison of 4f-SPAR versus the ‘no filtering’ and SBMIR algorithms. The test-images chessboard and Lena are used for the phase and amplitude modulation. The phase mask imitates the multiple plane phase retrieval scenario.

| Object \ Algorithm | 4f-SPAR | ‘no filtering’ | SBMIR |
|--------------------|---------|----------------|-------|
| Chessboard (phase) | .026 | .050 | fail |
| Chessboard (ampl) | .0063 | .029 | .075 |
| Lena (phase) | .026 | .042 | fail |
| Lena (ampl) | .019 | .03 | .072 |

Table 2. RMSE values for amplitude and phase reconstructions. Comparison of 4f-SPAR versus the ‘no filtering’ and SBMIR algorithms. The test-images chessboard and Lena are used for the phase and amplitude modulation. The random phase mask is used for the wave field modulation.

| Object \ Algorithm | 4f-SPAR | ‘no filtering’ | SBMIR |
|--------------------|---------|----------------|-------|
| Chessboard (phase) | .0068 | .044 | fail |
| Chessboard (ampl) | .0059 | .020 | .047 |
| Lena (phase) | .020 | .045 | fail |
| Lena (ampl) | .013 | .019 | .046 |

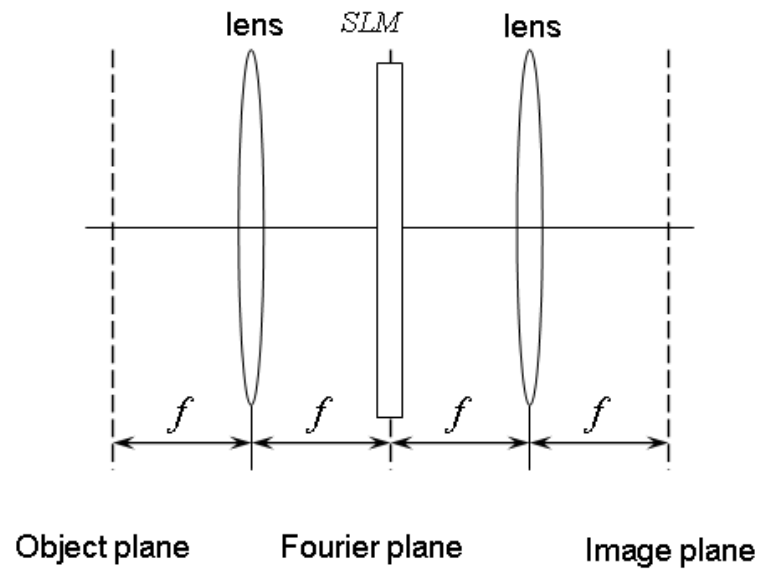


Fig. 1. $4f$ optical system: object, Fourier and image planes are in-focus of two lenses, optical mask (SLM) in Fourier focus plane of first lens.

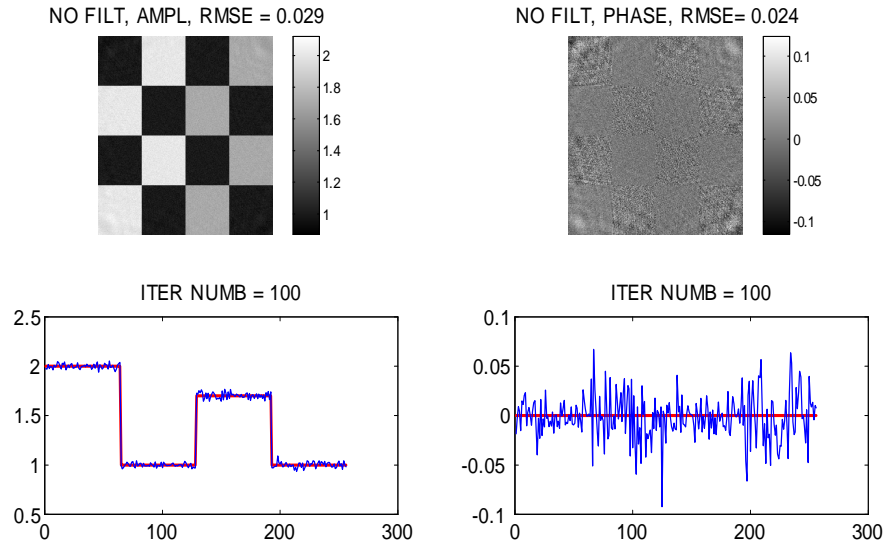


Fig. 2. The amplitude modulation object with the binary phase (chessboard test-image). The reconstruction by the ‘*no filtering*’ algorithm without phase/amplitude filtering. In the cross-sections thick (‘red’ in color) and thin (‘blue’ in color) lines show the true signal and the reconstructions, respectively. RMSE values for the phase and amplitude are shown at the top. The visual quality of the reconstruction is quite poor: noise, wiggles, waves, etc. are clearly seen.

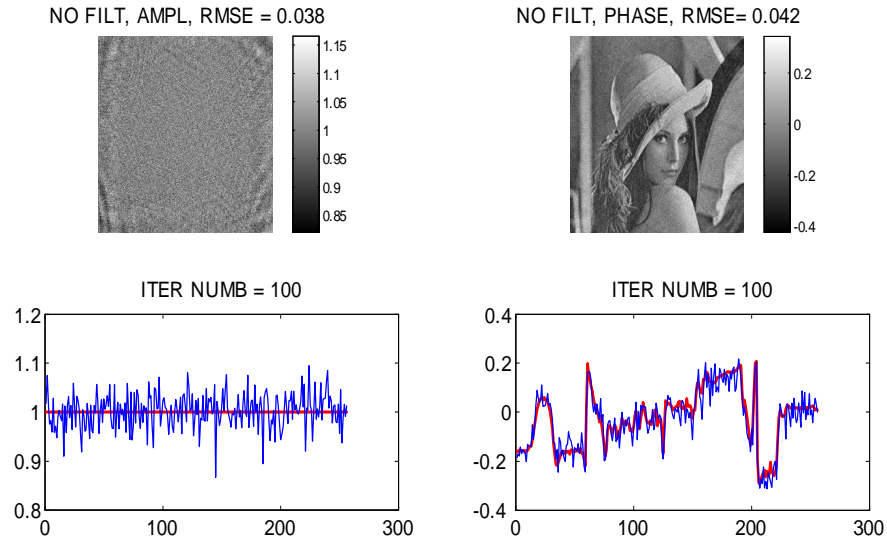


Fig. 3. The phase modulation object with the Lena test-image. The reconstruction by the ‘*no filtering*’ algorithm without phase/amplitude filtering. The visual quality of the reconstruction is quite poor: noise, wiggles, waves, etc. are clearly seen.

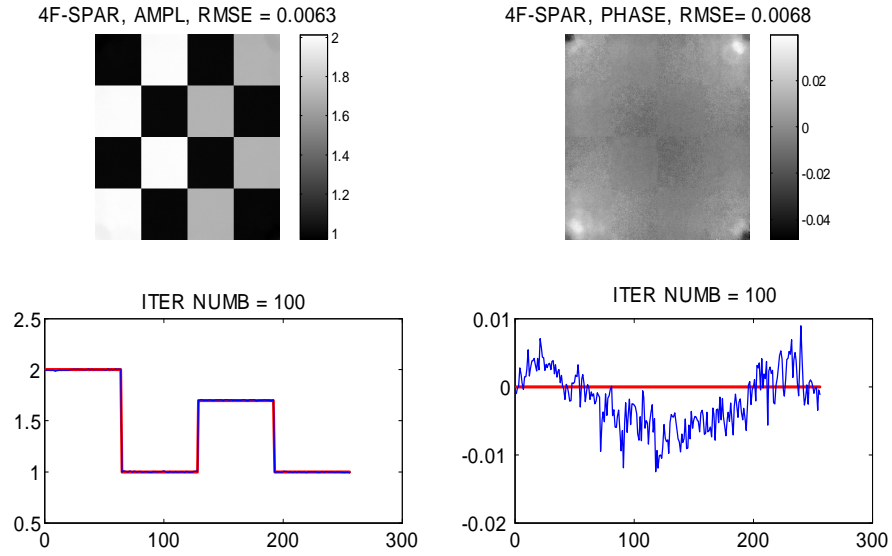


Fig. 4. The amplitude modulation object with the binary phase (chessboard test-image). The reconstruction by the 4f-SPAR algorithm. The visual quality of the reconstruction is very good, noise and diffraction artifacts are wiped out. Compare with Fig. 2, where the filtering is not used.

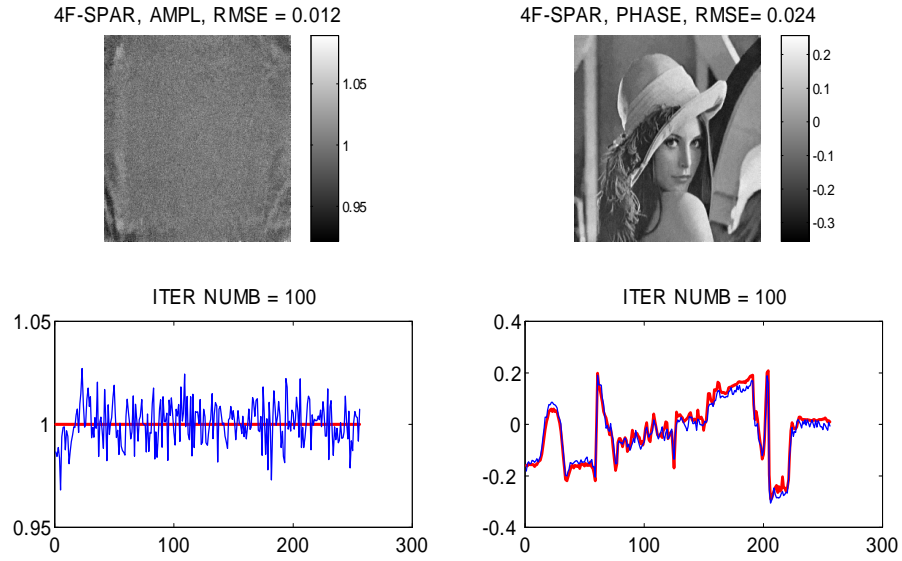


Fig. 5. The phase modulation object with the Lena test-image. The reconstruction by the 4f-SPAR algorithm. The visual quality of the reconstruction is very good, in particular versus Fig.3, where the filtering is not used.

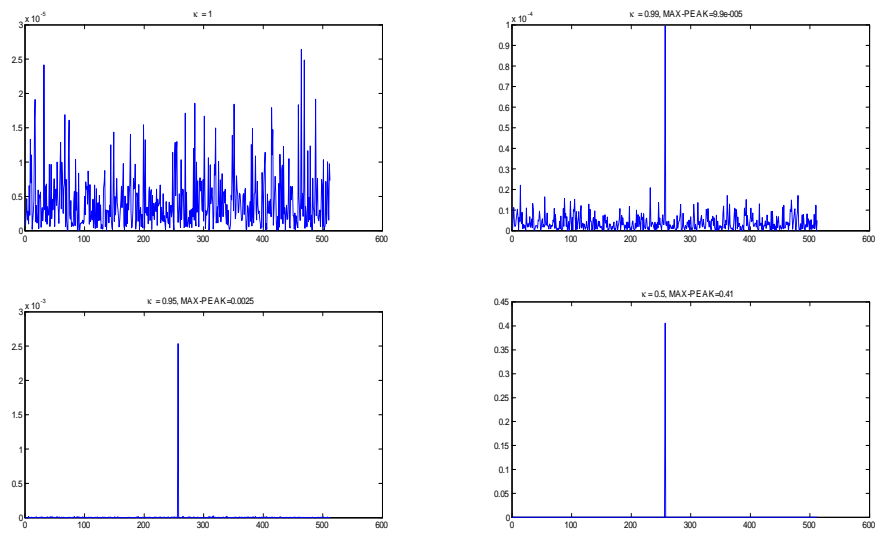


Fig. 6. Cross-sections of $\text{abs}^2(\tilde{m}_r)$ for $\kappa = 1.0, 0.99, 0.95, 0.5$.